nature communications

Article

https://doi.org/10.1038/s41467-023-41924-0

Structural insights into the conformational changes of BTR1/SLC4A11 in complex with PIP_2

Received: 11 April 2023

Accepted: 25 September 2023

Published online: 03 October 2023

Check for updates

Yishuo Lu[1,2,6], Peng Zuo[3,6], Hongyi Chen[1,2], Hui Shan[1], Weize Wang[2,3], Zonglin Dai[3], He Xu[4], Yayu Chen[4], Ling Liang[3,5], Dian Ding[1,3], Yan Jin[3] & Yuxin Yin[1,2,3]

BTR1 (SLC4A11) is a NH_3 stimulated H^+ (OH^-) transporter belonging to the SLC4 family. Dysfunction of BTR1 leads to diseases such as congenital hereditary endothelial dystrophy (CHED) and Fuchs endothelial corneal dystrophy (FECD). However, the mechanistic basis of BTR1 activation by alkaline pH, transport activity regulation and pathogenic mutations remains elusive. Here, we present cryo-EM structures of human BTR1 in the outward-facing state in complex with its activating ligands PIP_2 and the inward-facing state with the pathogenic R125H mutation. We reveal that PIP_2 binds at the interface between the transmembrane domain and the N-terminal cytosolic domain of BTR1. Disruption of either the PIP_2 binding site or protonation of PIP_2 phosphate groups by acidic pH can transform BTR1 into an inward-facing conformation. Our results provide insights into the mechanisms of how the transport activity and conformation changes of BTR1 are regulated by PIP_2 binding and interaction of TMD and NTD.

SLC4 transporters play essential roles in regulating intracellular pH (pHi) and other physiological processes such as CO_2 transport by erythrocytes and solute secretion/reabsorption across epithelia[1]. SLC4A11 (or BTR1, NaBC1) is a member of the SLC4 transporter family which was first classified and named as bicarbonate transporter-related protein-1 (BTR1) because of its sequence homology with other SLC4 family transporters[2]. However, unlike other SLC4 family members, BTR1 does not transport bicarbonate[2,3]. In contrast, based on its sequence similarity with the Arabidopsis borate transporter BOR1, BTR1 was first thought to function as an electrogenic, voltage-regulated, Na^+-$B(OH)_4^-$ coupled transporter and was renamed as NaBC1[3]. BTR1 was subsequently shown to have NH_3/H^+ electrogenic co-transport activity, which was atypical among SLC4 bicarbonate transporters[4]. This $NH_3/H(n)^+$ co-transport activity of BTR1 was independently corroborated by subsequent investigations[5,6]. However, as H^+ conductance of BTR1 is stimulated by alkaline pH and NH_3 is difficult to measure, whether NH_3 co-transport with H^+ is still in debate.

Like other SLC4 family transporters, BTR1 is widely expressed in kidney, salivary glands, testis, thyroid glands, and trachea[2,7,8]. In addition, BTR1 has been detected throughout the endothelial cell layer of cornea and the audio-vestibular system[9]. Given the uncertain influence of microelement borate homeostasis on the human body, apparent changes in pH_i and osmotic pressure are more likely to underlie *SLC4A11*-mutation associated diseases such as congenital hereditary endothelial dystrophy (CHED)[10–12], Fuchs' endothelial corneal dystrophy (FECD)[13] and Harboyan syndrome (or corneal dystrophy and perceptive deafness, CDPD)[14]. More than 60 disease-associated mutations in *SLC4A11* have been reported[15]. These diseases occur during different stages of life, but collectively, they are all associated with impaired vision or hearing. In addition to corneal transplantation, proposed

[1]Institute of Precision Medicine, Peking University Shenzhen Hospital, Shenzhen 518036, China. [2]Peking-Tsinghua Center for Life Sciences, Peking University, Beijing 100871, China. [3]Institute of Systems Biomedicine, Department of Pathology, Beijing Key Laboratory of Tumor Systems Biology, School of Basic Medical Sciences, Peking University Health Science Center, Beijing 100191, China. [4]XtalPi, Beijing, China. [5]Department of Biochemistry and Biophysics, School of Basic Medical Sciences, Peking University Health Science Center, Beijing 100191, China. [6]These authors contributed equally: Yishuo Lu, Peng Zuo.
e-mail: yinyuxin@hsc.pku.edu.cn

treatment involves the restoration of the ER mis-localized mutant BTR1 to its normal membrane localization[16]. However, there are currently no treatments available that target mutant BTR1 with altered function. For this reason, solving the structure of BTR1 and understanding the mechanism of its transport activity are extremely important for gaining insights into therapeutic strategies to approach certain BTR1-related diseases.

In recent years, several structures of SLC4 family transporters have been reported, such as the crystal and cryo-EM structures of human[17–19], bovine[20] AE1 (SLC4A1), recently solved cryo-EM structures of AE2 (SLC4A2)[21], cryo-EM structures of NBCe1 (SLC4A4)[22] and NDCBE (SLC4A8)[23]. These structures describe the protein interactions[18,19], the substrates binding sites[17,18,21–23], the inhibitor binding sites[17,21] and provide explanations for the consequences of certain pathogenic mutations[17,18,22] and the regulatory mechanism of transport activity[21]. However, these structures did not resolve the complete NH_2-terminal domains (NTDs), which leaves a critical gap in our understanding of the interaction(s) between the NTDs and TMDs of these SLC4 transporters. These prompted us to explore the relationship between the NTD and TMD of SLC4 transporters, and how it is influenced by pH.

Here, we have used single-particle cryo-EM to determine human BTR1 full-length structures in the outward-facing states with and without addition of ammonia at resolutions of 2.94 Å and 2.84 Å, respectively. We also describe the inward-facing structures of BTR1 containing the pathological mutation R125H, and BTR1 under acidic pH conditions at resolutions of 2.96 Å and 2.94 Å, respectively. These structures reveal that the interaction between the NTD and TMD of BTR1 in the outward-facing state is mainly mediated by PIP_2, the key regulator of BTR1 activity, as well as how disease-associated mutations disrupt BTR1 function. Our work provides insights into the regulatory mechanisms of BTR1 and other SLC4 transporters.

Results

Cryo-EM structure of BTR1 in the outward-facing state

For structural and electrophysiological studies, full-length human BTR1, fused with a C-terminal green fluorescent protein (GFP) and a His8 tag, was expressed in FreeStyle HEK293F cells[24]. Whole-cell patch clamp approach was used to measure the H^+ conductance of cells transfected with recombinant BTR1 or empty vector (EV) (Fig. 1a and Supplementary Fig. 1). No currents were observed in cells transfected with EV during NH_4Cl exposures (Supplementary Fig. 1a–d) whereas NH_4Cl exposures induced apparent inward currents of cells transfected with recombinant BTR1 (Fig. 1a and Supplementary Fig. 1e, f) accompanied by a shift in zero-current potentials from −17 mV to −4 mV (Fig. 1a), which is similar as previous study[6]. Recombinant BTR1 overexpressed in FreeStyle HEK293F cells was purified in Glycodiosgenin (GDN) detergent-solubilized micelles (Supplementary Fig. 1g, h) and then subjected to cryo-EM analysis. Structures of BTR1 with the addition of NH_4Cl ($BTR1_{OF/NH3}$ state) and in the apo state ($BTR1_{OF/APO}$ state) were resolved at resolutions of 2.84 Å and 2.94 Å, respectively (Supplementary Fig. 2).

These BTR1 structures reveal an outward-facing dimeric architecture with each monomer containing a TMD (residues 336–891) and a cytoplasmic domain (NTD) (residues 1–307). The TMD contains a core domain (comprising TMs 1–4 and 8–11) and a gate domain (comprising TMs 5–7 and 12–14) (Fig. 1b), resembling the arrangement

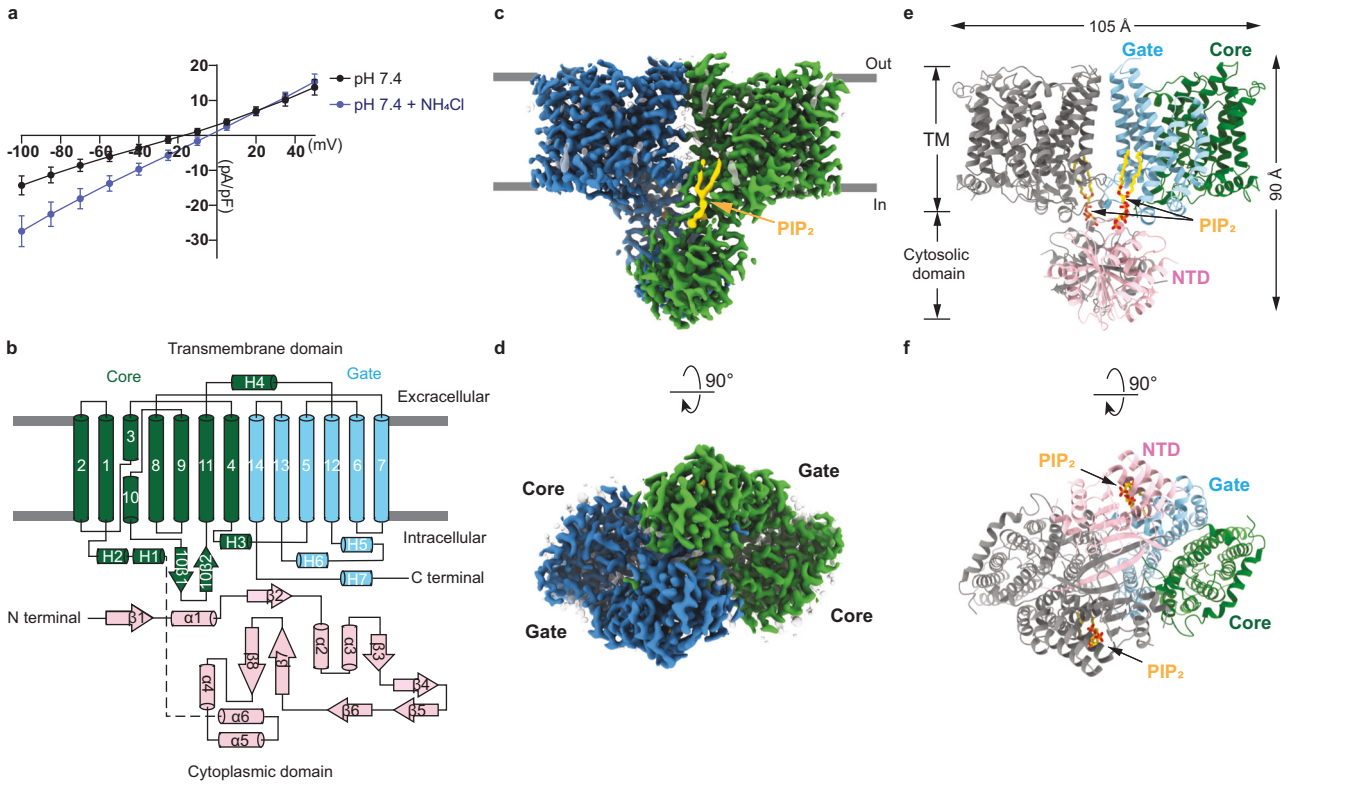

Fig. 1 | Cryo-EM structure of BTR1 in the outward-facing state. a *I*–*V* curve of cells expressing wild-type BTR1 at pH 7.4 in the presence and absence of 5 mM NH_4Cl. The current values are standardized by cell capacitance. Data shown are mean values ± s.d. of $n = 4$ biologically independent experiments. **b** Topology and domain arrangement of a BTR1 monomer. The gate domain, core domain and N-terminal cytoplasmic domain (NTD) are shown in blue, green and pink, respectively. Gray bars represent the boundaries of the cell membrane. **c**, **d** Cryo-EM maps of the outward-facing state of a BTR1 dimer bound to PIP_2: views from the side (**c**) and the bottom (**d**). The two monomers of BTR1 are colored in blue and green, and the PIP_2 molecules are colored in gold. The remaining lipid molecules are shown as transparent gray. **e, f** Structural model of the outward-facing state BTR1 views from the side (**e**) and the bottom (**f**). The two PIP_2 molecules are shown in stick representations. The color scheme of one BTR1 monomer is the same as in (**b**), and the other monomer is colored in gray.

of UraA[25]. In the outward-facing state, the BTR1 dimer occupies a 3D space of ~105 Å × 65 Å × 90 Å (Fig. 1c–f). The TMD of BTR1 in the outward-facing state closely resembles the structures of SLC4 family members AE1 (pdb 4YZF) (Supplementary Fig. 3a)[17], NBCe1 (pdb 6CAA) (Supplementary Fig. 3b)[22] and NDCBE (pdb 7RTM) (Supplementary Fig. 3c)[23] with RMSDs of 1.860 Å, 1.780 Å and 2.180 Å, respectively. The formation of a dimeric TMD mainly depends on the interaction of the loop between H5 and H6 helix of one monomer and the loop between TM6 and TM7 of the other monomer in the gate domain (Supplementary Fig. 3d). In addition, the hydrophobic interactions occur in TM5, TM6, and TM7 of the two monomers also promote the formation of dimeric TMDs (Supplementary Fig. 3e). The formation of dimeric NTDs mainly relies on the hydrogen bonds between the β1 sheets of the two monomers (Supplementary Fig. 3f). Finally, the TMD and NTD interact through the electrostatic interactions of PIP_2 with the residues in the PIP_2 binding pocket. Additionally, the hydrophobic interaction between I124 and P825, as well as the electrostatic interactions between E122 and R823, E123 and R822 assist in the association of the TMD and NTD (Supplementary Fig. 3g).

Substrate binding sites of BTR1

Previous studies proposed that BTR1 is a H^+ transporter[4–6]. BTR1 shares a similar membrane topology with other SLC4 family members, with its substrate binding sites located in the central cavity between the gate and core domains. Negative charges in TM1, TM3, TM5, TM8 and TM10 suggest that residues in these helices contribute to the H^+ binding site (Fig. 2a, b). We analysed the pore dimensions of the transmembrane domains using HOLE2[26]. The results show that the substrate binding sites of $BTR1_{OF/APO}$ and $BTR1_{OF/NH3}$ are accessible from the extracellular side (Fig. 2c, d), confirming their outward-facing conformation. In the cryo-EM map of $BTR1_{OF/NH3}$ state, we identified two densities with relatively different intensity from the $BTR1_{OF/APO}$ state in the substrate binding sites and both states reveal several extra densities (represented by Molecule 1–6), distribute along TM5 and the ion permeation pathway lined up by residues F393, L396, G509, D505, T501 and I498 (Supplementary Fig. 3h–j). These densities could be either waters or ammonia. However, lack of details of the densities precludes the further determination of their identities. In our BTR1 outward-facing state model, pathogenic mutations H724A and E675Q[15,27,28] are located at the substrate binding site and near the extra densities (Supplementary Fig. 3h). E675 of BTR1 is partly conserved among human SLC4 family members and BTR1 orthologs (Fig. 2e–h, j). M3 (Molecule 3) could be fixed by the formation of hydrogen bonds between the side chain of E675 and the backbones of A720 and Y722 (Supplementary Fig. 3h). This negatively charged amino acid may participate in the coordination of H^+ during substrates transport process of BTR1, as the corresponding D800 of NDCBE forms ionic bond with Na^+ (Fig. 2h) and the substitution of this residue significantly impairs the activity of SLC4 family transporters[17,22,23]. P437 is highly conserved among human SLC4 transporters and BTR1 orthologs, but P723, H719 and H724 are only conserved among BTR1 orthologs (Fig. 2e–h, j), which may be responsible for the atypical substrate selectivity of BTR1. M5 and M6 are both located at the substrate binding pocket and M5 could form hydrogen bond with the backbone carbonyl group of T434 (Supplementary Fig. 3h). M2 at the entrance of the binding pocket may form hydrogen bond with D505. Extracellular proton may be attracted by the core domain and delivered to D505, then transferred through proton carriers including water or ammonia molecules, and finally released by E675. Molecules in the binding pocket of $BTR1_{OF/NH3}$ may be associated with the hydration of the pocket and could be utilized for proton transportation.

To investigate the effects of specific amino acids at the substrate binding site on BTR1 transport activity, a series of point mutations were introduced into BTR1 and expressed in HEK293F cells. The BTR1 mutants traffic to the cell membrane surface with little or indistinguishable differences from wild-type BTR1-HA (Supplementary Fig. 4a, b). Furthermore, the electrophysiological experiments show that P723A, H724A and H719A-H724A mutations partially attenuate the NH_3 stimulated H^+ currents, especially at higher NH_3 concentration, while E675Q mutation almost eliminates the NH_3 stimulated H^+ currents (Fig. 2i). These observations confirm P723, H719, H724 and the negatively charged E675 contribute to BTR1's unique transport activity of proton which could be stimulated by NH_3.

Interaction between PIP_2 and NTD is essential for the substrate transport process of BTR1

PIP_2 has been widely reported to function as an intracellular phosphoinositide regulator[29], which can regulate the activity of channels[30] and transporters[31,32], including the SLC4 family transporters NBCe1 (SLC4A4)[33,34] and NBCn1 (SLC4A7)[35]. Because of the high resolution of BTR1 structures, we were able to identify the density which clearly shows the molecular features of PIP_2 (Figs. 1c and 3b, c). PIP_2 molecules were derived from BTR1 expressing HEK293F cells. The two phospholipid tails of PIP_2 interact with the H5 helix and TM13 of the TMD through hydrophobic interactions (Supplementary Fig. 4c). Moreover, the inositol head of PIP_2 is surrounded by a positively charged pocket formed by TM13 of the TMD as well as by the α1 helix, the loop between the β3 and β4 sheets and the loop between the β5 sheet and the α4 helix of the NTD (Fig. 3a–c). We termed the involving charged residues R125, R128, R227, K260, K263, R827 and polar residue Q826 together as the lipid binding site (L site). These residues form extensive electrostatic interactions with the phosphate groups of PIP_2 inositol head (Fig. 3b, c). We next performed molecular dynamics simulations with the $BTR1_{OF/APO}$ state structure. During a 1 μs simulation, the overall structure of BTR1 gradually stabilizes (Supplementary Fig. 4d). In this process, PIP_2 still binds stably with BTR1, as the relative distances between the phosphate groups of PIP_2 and the adjacent amino acid side chains remain low (Supplementary Fig. 4e). We also calculated the binding free energy of one molecule of PIP_2 binding to BTR1 using MM/GBSA[36]. The value obtained is −100.66 kcal/mol that confirms the stability of PIP_2 binding. Structural alignment of the $BTR1_{OF/APO}$ state with AE1 (pdb 8CT3) by the gate domain shows that PIP_2 molecules bind to different regions of these transporters (Fig. 3d), which indicates that PIP_2 plays a different role in the entire transport processes of AE1 and BTR1.

As noted earlier, loss of function of BTR1 caused by the R125H mutation has been widely reported[9,37]. R125 is conserved among BTR1 orthologs but not among the SLC4 family members (Fig. 3e). Given that the binding of PIP_2 is pH sensitive and histidine is less positively charged than arginine under physiological pH conditions, we presume that the pathogenesis of R125H mutation can be attributed to the charge alteration of the L site which in turn adversely affects the binding of PIP_2, ultimately leading to the impaired transport activity of BTR1. We performed the mutations of R125, R128, R227, K260 and K263 in the L site and measured the NH_4Cl stimulated currents, respectively. All these mutants traffic normally (Supplementary Fig. 4b). The electrophysiology experiments results confirm that the R125H mutation attenuates the transport activity of BTR1 (Fig. 3f), which is consistent with previous studies[6,37]. NH_3 stimulated currents of K260A and K263A mutants are also significantly reduced at extracellular pH (pHe) 7.4 and 8.0 (Fig. 3f). Previous studies have reported that the transport activity of BTR1 is enhanced by intracellular alkalization, but the enhancement is abolished by R125H mutation[38,39]. Thus, we hypothesize that PIP_2 molecules participate in the pH sensing process of BTR1 through passively changing their binding affinity with BTR1 under alkaline or acidic pH. Therefore, we measured the NH_3 stimulated currents of wild-type BTR1 and BTR1-R125H mutant at different intracellular pH (pHi) to test whether BTR1 with disrupted PIP_2 binding site is more sensitive to acidic pH. The electrophysiology experiment results show that the current densities of wild-type BTR1

https://doi.org/10.1038/s41467-023-41924-0

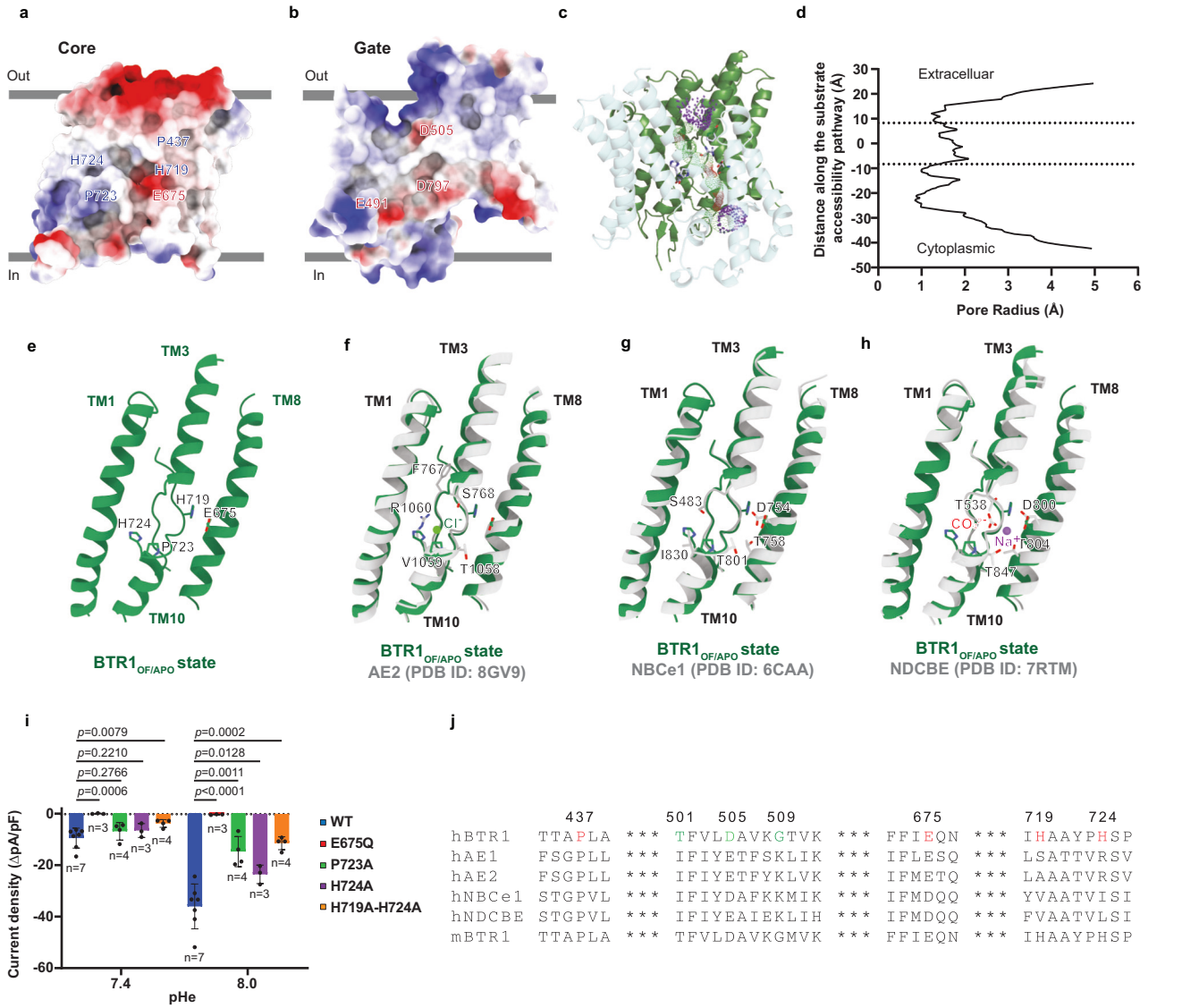

Fig. 2 | Substrates binding sites of BTR1. a, **b** Electrostatic surface representation of the core domain (**a**) and gate domain (**b**) of BTR1 in the outward-facing state. Functionally important amino acids are shown in blue or red according to their charge. **c**, **d** Ion permeation pathway of BTR1 in the outward-facing state conformation (**c**) and the pore radius values along the pathway (**d**). The dotted lines represent the extracellular and intracellular borders of the substrate binding site. The gate domain and core domain are colored in blue and green, respectively. The analyses were performed using HOLE2. **e** Substrate binding pocket of $BTR1_{OF/APO}$. The residues participating in the substrates coordination of BTR1 are labeled. **f**–**h** Alignment of the substrate binding pocket of $BTR1_{OF/APO}$ with AE2 (PDB ID: 8GV9) (**f**), NBCe1 (PDB ID: 6CAA) (**g**) and NDCBE (PDB ID: 7RTM) (**h**). The residues participating in the substrates coordination of AE2, NBCe1 and NDCBE are labeled. The Cl^- ion was shown as green sphere in (**f**). The CO_3^{2-} ion and Na^+ ion were shown as stick model and purple sphere in (**h**), respectively. **i** Functional analysis of the residues involved in the substrate binding pocket formation. The current density values were calculated by the extreme difference of the current values after addition of 5 mM NH_4Cl at extracellular pH (pHe) 7.4 and 8.0. The current values are standardized by cell capacitance. Data shown are mean values ± s.d. of n biologically independent experiments and *p*-values were calculated by two-sided unpaired *t*-tests. **j** Sequence alignment of the residues in the pore region from *Homo sapiens* BTR1, *Homo sapiens* AE1, *Homo sapiens* AE2, *Homo sapiens* NBCe1, *Homo sapiens* NDCBE and *Mus musculus* BTR1 by PROMALS3D. Amino acids which are important for substrates coordination and permeation pathway formation are colored in red and green respectively.

hardly change as pHi dropped from 7.4 to 7.0. However, those of BTR1-R125H mutant are significantly reduced (Fig. 3g). This difference indicates that robust PIP_2 binding can enhance the tolerance of BTR1 to intracellular acidification, which is consistent with our hypothesis.

In summary, our data demonstrate that PIP_2 binds in the positively charged pocket formed by the TMD and NTD of BTR1 and plays essential roles in the complete substrate transport process of BTR1.

BTR1 adopts inward-facing conformation in the absence of PIP_2

To further explore how PIP_2 participates in the complete substrate transport process of BTR1 and prove the connection between PIP_2 and pH sensing, we attempted to solve the structures of BTR1 with the R125H mutation or wild-type BTR1 prepared under acidic pH, which may both disrupt the interaction between BTR1 and PIP_2, and succeed in achieving resolutions of 2.96 Å and 2.94 Å, respectively (Supplementary Fig. 5). Intriguingly, two structures are nearly indistinguishable in conformation (RMSD = 0.250 Å) (Supplementary Fig. 6a), and both lack the densities of PIP_2. These results suggest that the disruption of PIP_2 binding site and acidic pH can both lead to the dissociation of PIP_2. Non-PIP_2 binding BTR1 occupies a 3D space of ~100 Å × 55 Å × 85 Å (Fig. 4a, b). Compared with the structures of BTR1 in the outward-facing state, the distinct features of the non-PIP_2 binding BTR1 structures involve that the NTD has undergone a significant twist, as well as an apparent conformational change has taken place in the

https://doi.org/10.1038/s41467-023-41924-0

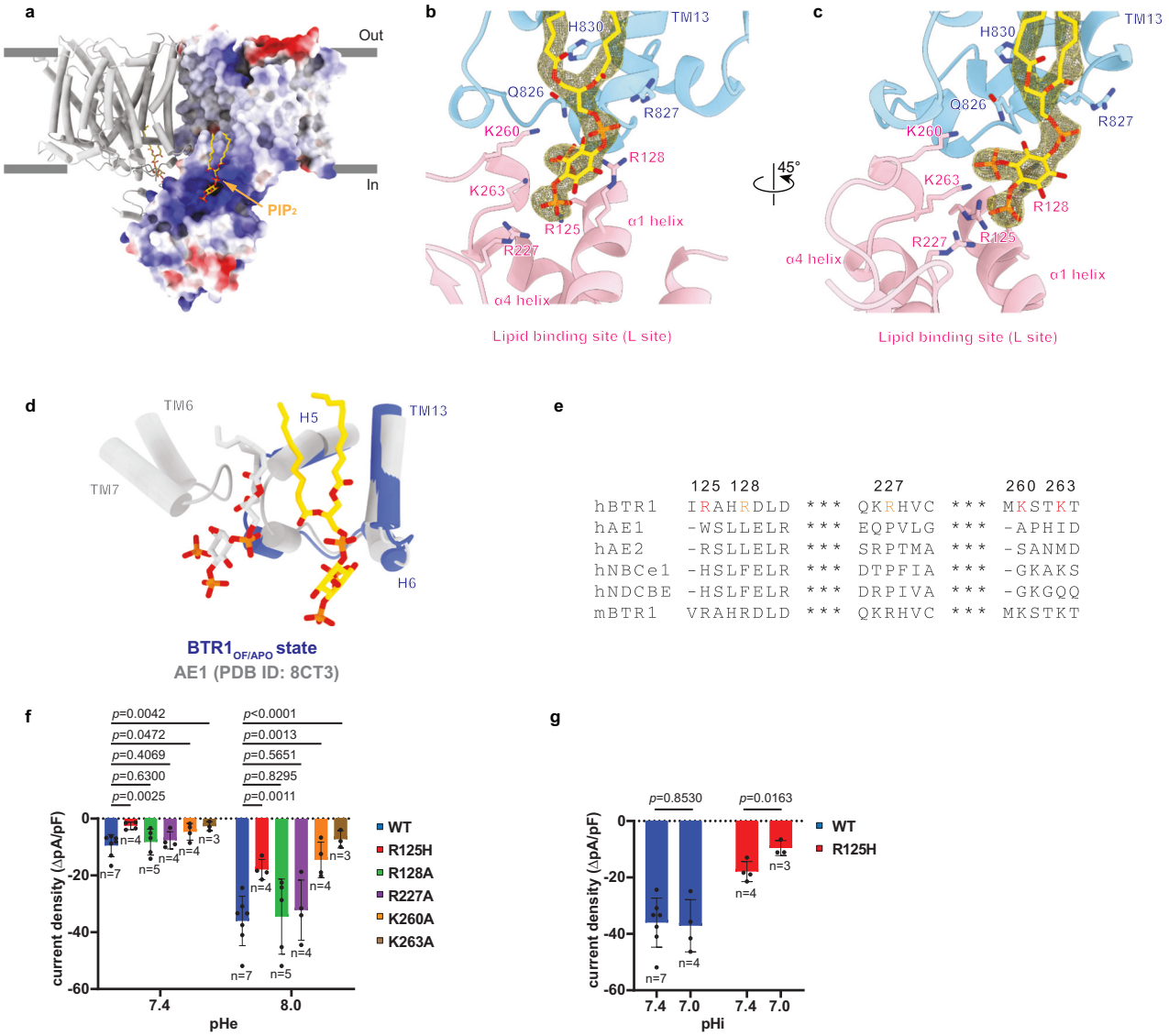

Fig. 3 | PIP$_2$ binding site of BTR1 in the outward-facing state. a BTR1$_{OF/APO}$ dimer with one monomer shown as electrostatic surface representation. PIP$_2$ molecules are shown as gold sticks. **b**, **c** Close-up views of the PIP$_2$ binding site. The PIP$_2$ density is shown in mesh. The PIP$_2$ molecule and its surrounding residues are shown in stick representation. TMD, NTD and PIP$_2$ are colored in blue, pink and gold, respectively. **d** Structural comparison of the PIP$_2$ binding sites of BTR1$_{OF/APO}$ (blue, with PIP$_2$ colored in gold) and AE1 (gray, with PIP$_2$ colored in gray) (PDB ID: 8CT3) aligned by the gate domains. Helices of BTR1 and AE1 are labeled in blue and gray, respectively. **e** Sequence alignment of the NTD residues forming the PIP$_2$ binding site from *Homo sapiens* BTR1, *Homo sapiens* AE1, *Homo sapiens* AE2, *Homo sapiens* NBCe1, *Homo sapiens* NDCBE and *Mus musculus* BTR1. Residues that are important for PIP$_2$ coordination and involved in forming the PIP$_2$ binding pocket (L site) are colored in red and orange, respectively. **f** Functional analysis of the residues in the PIP$_2$ binding site. The current density values of wild-type and mutant BTR1 proteins after the addition of 5 mM NH_4Cl at pHe 7.4 and 8.0 as measured by whole-cell patch-clamp. Data shown are mean values ± s.d. of n biologically independent experiments and *p*-values were calculated by two-sided unpaired *t*-tests. **g** The current density values of wild-type BTR1 and BTR1-R125H proteins at different intracellular pH (pHi 7.0 and 7.4), measured by whole-cell patch-clamp. Data shown are mean values ± s.d. of n biologically independent experiments and *p*-values were calculated by two-sided unpaired *t*-tests.

TMD. Analysis of the TMDs using HOLE2 shows that the substrate binding sites of BTR1 in these two states are accessible from the intracellular side (Fig. 4c, d), suggesting their inward-facing conformation.

The structural alignment of the TMDs of BTR1$_{OF/APO}$ state and BTR1$_{IF/R125H}$ state by the gate domains shows that, during the conformation transition process from the outward-facing state to the inward-facing state, the gate domains remain relatively unchanged (RMSD = 1.678 Å), but an obvious displacement has occurred in the core domains (RMSD = 3.784 Å) (Fig. 4e, f and Supplementary Fig. 6e). In specific, the core domain of BTR1 has gone through a movement vertically towards the cytoplasm and horizontally towards the dimer interface (Fig. 4e, f). As for the gate domain, only H6 and H7 helices shift towards the dimer interface to a certain extend (Fig. 4g). The core domain of BTR1$_{OF/APO}$ state needs to go through a 12.38° rotation and a 7.4 Å shift towards the gate domain to reach the position of core domain of BTR1$_{IF/R125H}$ state. The pore region formed by TM1, TM3, TM8 and TM10 has undergone similar movements. We define the centroid of P437 and P723 as the center of the pore region and observe that the centroid has moved 4.23 Å during the state transition process by aligning the gate domains (Fig. 4h). Alignment of the core domains and gate domains of BTR1$_{OF/APO}$ state and BTR1$_{IF/R125H}$ state separately show that the TMs arrangements within the core domain (RMSD = 1.093 Å) (Supplementary Fig. 6b) and the gate domain (RMSD = 0.547 Å) (Supplementary Fig. 6c) change slightly. These features are consistent with the previous studies which propose that SLC4 family

https://doi.org/10.1038/s41467-023-41924-0

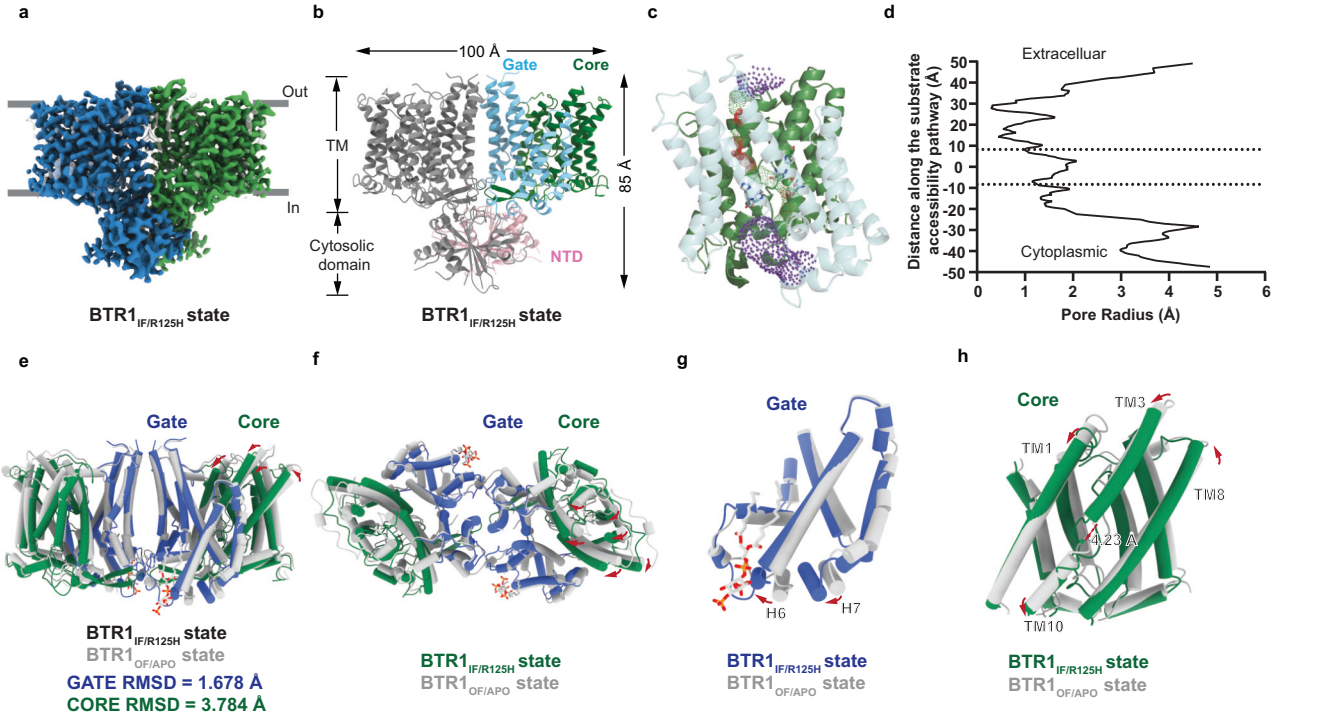

Fig. 4 | TMDs of BTR1 in the inward-facing conformation. a, **b** Cryo-EM map and structural model of the BTR1 dimer in the inward-facing state as viewed from the side. The color schemes are the same as in Fig. 1 (**c**–**e**). **c**, **d** Ion permeation pathway of BTR1 in the inward-facing state conformation (**c**) and the pore radius values along the pathway (**d**). **e**, **f** Structural alignment of TMDs of $BTR1_{IF/R125H}$ and $BTR1_{OF/APO}$ as viewed from the side (**e**) and the bottom (**f**). The shift directions of the transmembrane helices when transitioning from the outward-facing state to the inward-facing state are shown as red arrows. The alignment RMSDs of the gate domains and core domains are labeled below. **g** Structural alignment of the gate domains of $BTR1_{IF/R125H}$ and $BTR1_{OF/APO}$. The helices with marked displacement are labeled in black. The shift direction of helices are shown as red arrows. **h** The centroid shift of the pore region during the state transition process. The centroids of residues P437 and P723 of $BTR1_{IF/R125H}$ and $BTR1_{OF/APO}$ are shown as green and gray spheres, respectively. The centroid shift is shown as red dotted arrow. The shift direction of helices are shown as red arrows.

transporters implement the elevator-like transport mechanism[20,40,41]. Similar displacements of the core domain have been observed in some transporters of other families which execute the elevator-like mode transportation, including NHE1 (~10° rotation of the core domain, 5 Å displacement of the Cα of D267)[42] and PIN8 (~20° rotation of the core domain, 5 Å displacement of the substrate binding site)[43]. These results support that BTR1 acts by the elevator mechanism.

NTD of BTR1 in the inward-facing conformation

In comparison with the alteration of the TMD caused by the disruption of the interaction between PIP_2 and BTR1 during the state transition process, the conformation of the NTD changes even more significantly. The NTD has undergone a 175.9 ° deflection and a 24.9 Å position shift from $BTR1_{OF/APO}$ state to $BTR1_{IF/R125H}$ state conformation (Fig. 5a, b).

Intriguingly, the arrangement of the dimeric NTD of the $BTR1_{OF/APO}$ state is similar as that of the $BTR1_{IF/R125H}$ state with a RMSD of 1.848 Å (Fig. 5c). In the absence of PIP_2, residues which participate in the formation of the L site in the $BTR1_{OF/APO}$ state, have flipped to the cytosolic side of the whole frame (Fig. 5c). Densities of α1, the loop between α1 and β1 and the loop between α4 and β8 of BTR1, which can be clearly seen in the $BTR1_{OF/APO}$ state, disappear in the $BTR1_{IF/R125H}$ state due to the loss of interaction with PIP_2 and TMD (Supplementary Fig. 6d).

Meanwhile, the interface between the TMD and NTD of $BTR1_{IF/R125H}$ state has changed: the loop between β4 and β5 sheets, which is originally located at the bottom of the NTD and cannot be seen due to its flexibility in the $BTR1_{OF/APO}$ state, has flipped up to the top and interacts with H6 helix and the loop between H5 and H6 helices of the gate domain through hydrogen bonds (formed between V205 and Y820, Q212 and V739, E736 and S213) and extensive hydrophobic interactions (Fig. 5d, e). The mutual repulsion between R209 of β5 (only stable in the inward-facing state) and R738 of 10β1 leads to the 10β1 and 10β2 sheets of the core domains being pushed away from the gate domains by β4 and β5 of the NTDs (Fig. 5d), which may trigger the overall horizontal shift of the core domains compared with the outward-facing state. In addition, the electrostatic interaction between R282 and E736 as well as the hydrogen bonds formed between the gate domain and the loop between β7 and β8 of the other NTD (between R822 and T145, T813 and P237, N239 and T813, N239 and A814) further stabilize the interactions between the TMDs and NTDs of BTR1 in the inward-facing conformation (Fig. 5f). R822 of H6 helix, which interacts with the NTD within a BTR1 monomer in the outward-facing state, turns to interact with the loop between α1 and α2 helixes (T146) in the NTD of the other monomer (Fig. 5f).

In short, the NTDs of $BTR1_{OF/APO}$ state turns nearly upside down due to loss of interaction with PIP_2, which further facilitate the transition of TMDs and establish new interactions with TMDs to stabilize BTR1 in the inward-facing conformation.

Discussion

Despite BTR1 was first named as bicarbonate transporter-related protein-1 because of its sequence homology with the transporters of the SLC4 family, it does not transport bicarbonate like other family members. There is debate about whether NH_3 co-transport with H^+ or NH_3 activate H^+ transport activity. High-resolution maps of $BTR1_{OF/APO}$ state and $BTR1_{OF/NH3}$ state allow us to unambiguously identify the side chains of residues in the substrate coordination site. The mutagenesis analysis results show that H719, H724 and P723, which are not conserved among the SLC4 family (Fig. 2e–h, j), participate in the substrate transport process and play important roles in the presence of high

https://doi.org/10.1038/s41467-023-41924-0

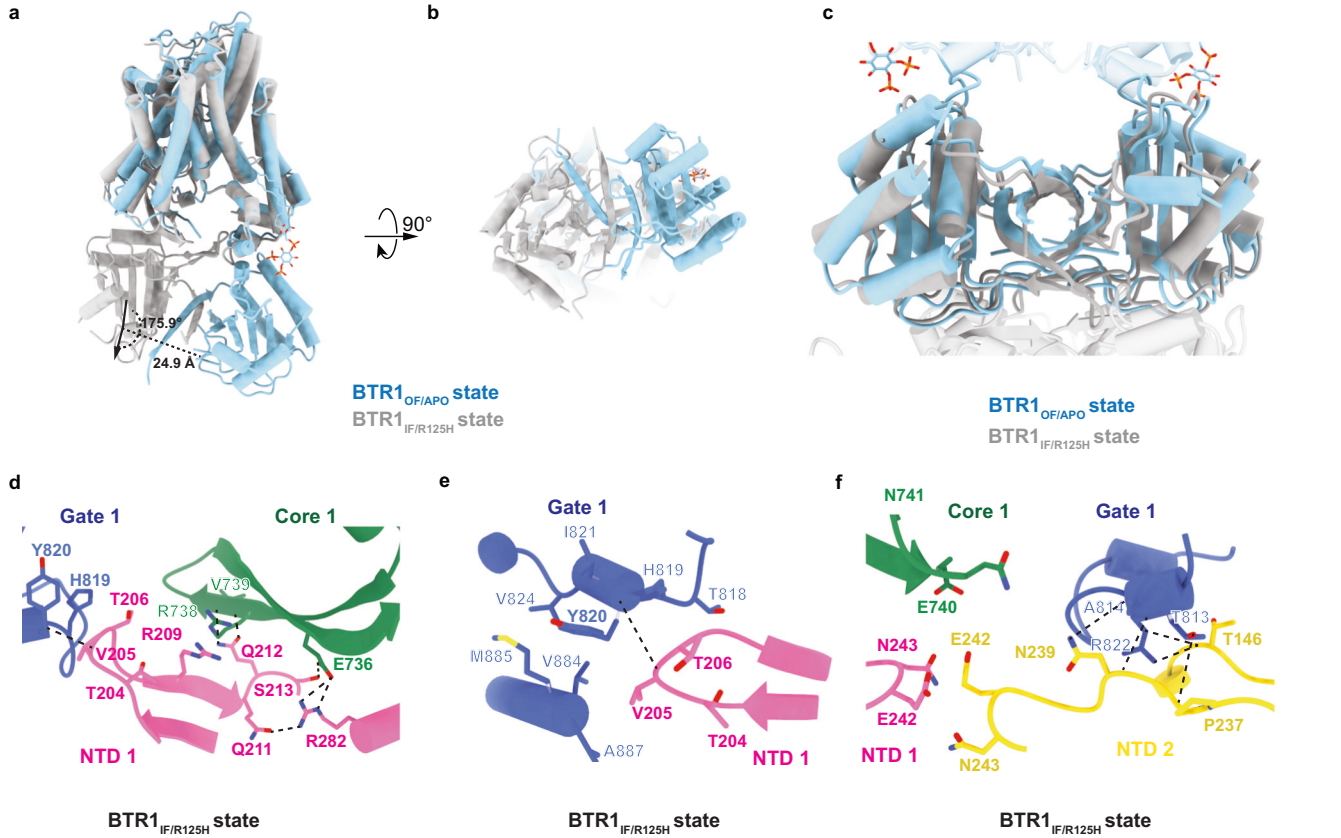

Fig. 5 | NTDs of BTR1 in the inward-facing conformation. a, **b** Structural comparison of $BTR1_{OF/APO}$ (blue) and $BTR1_{IF/R125H}$ (gray) monomers aligned by their TMDs viewed from the side (**a**) and the bottom (**b**). The rotation angle and centroid shift between $BTR1_{OF/APO}$ and $BTR1_{IF/R125H}$ are marked with dotted lines. **c** Structural comparison of $BTR1_{OF/APO}$ (blue) and $BTR1_{IF/R125H}$ (gray) aligned by their NTDs. The TMDs are both shown in transparent mode. **d** Hydrophobic interactions and hydrogen bonds formed between the NTD and TMD of one $BTR1_{IF/R125H}$ monomer. The NTD, gate domain and core domain of one $BTR1_{IF/R125H}$ monomer are colored in pink, blue and green, respectively. The interactions are shown as dotted lines. **e** Close-up view of the hydrophobic interactions between the NTD and gate domain of one $BTR1_{IF/R125H}$ monomer. The hydrophobic interaction between V205 and Y820 is shown as dotted lines. **f** Hydrogen bonds between the gate domain of one $BTR1_{IF/R125H}$ monomer and the NTD of the other monomer. The interactions are shown as dotted lines.

concentration of NH_3 (Fig. 2i). E675Q mutation totally abolishes the H^+ currents (Fig. 2i), which is consistent with the influences of the mutant counterparts of other SLC4 family transporters and can explain the pathogenic mechanism of this mutation. Though our structures cannot settle the dispute in this field, the densities along the substrate permeation pathway reveal the importance of the surrounding residues. We have also provided precise structure models for further functional studies and MD simulations.

Previous studies have reported that PIP_2 participate in the regulation of the transport activity of SLC4A4 and co-localize with SLC4A1[33,44,45]. Recently solved cryo-EM structures of prestin and band 3–ankyrin multi-protein complex are with the combination of cholesterol or PIP_2[19,46]. Prestin and AE1 are structurally similar to BTR1. The observed combination of cholesterol with the TMDs of prestin provides direct evidence that lipid can act as a regulatory element and play an essential role in the transporter function[46]. The combined PIP_2 in AE1 may participate, at least partially, in the recruitment of protein 4.2[19]. Our structure of $BTR1_{OF/APO}$ state is also in complex with PIP_2. Disruption of the PIP_2 binding sites ($BTR1_{IF/R125H}$ state) or acidic pH ($BTR1_{IF/5.5}$ state) both turn BTR1 into the inward-facing conformation. The conformational changes induced by the adjustment of pH have also been observed in recently solved AE2 structures[21]. The mutagenesis analysis prove the importance of R125H, K260A and K263A mutations in BTR1 substrates transport activity and BTR1 R125H mutant is more sensitive to acidic pH than wild-type BTR1. Previous studies have proposed that NH_3 activate BTR1 by inducing the alkalization of the intracellular environment[39], which can be achieved through the transport of BTR1 or diffusion across the cytoplasmic membrane. Here we suggest that PIP_2 may participate in sensing the intracellular pH by changing its affinity to BTR1. BTR1 with a disrupted PIP_2 binding site needs more alkaline pH to interact with PIP_2 to accomplish substrates transportation.

The transport mechanisms of transporters are divided into three categories: rocker switch, rocker bundle and elevator[47]. The transport process of the SLC4 family transporters has been widely considered as an elevator mode and the recently solved structures of AE1 in both inward-facing and outward-facing state further support the mechanism[20,25,40,41]. Through structural analysis, we also believe that BTR1 works in this mode and we propose the following model (Fig. 6). In the apo state, BTR1 binds to PIP_2 in a stable manner (Fig. 6a). PIP_2 molecules then dissociate from the NTD of BTR1 after ions reach the substrate binding sites, leading to the conformation of BTR1 changing into an inward-facing state or a state between inward-facing and outward-facing (occluded state) (Fig. 6b). Protonation of PIP_2 under acidic pathological condition or pathogenic mutations exist in the L site of BTR1 lead to the disruption of the interaction between PIP_2 and BTR1. The NTD dimer then turns upside-down and inserts β4 and β5 sheets into the gate domains and finally stabilizes BTR1 in the inward-facing conformation (Fig. 6c). Our model is in agreement with the recently solved structures of AE2 in different states regulated by pH[21] and supplement the pH-sensing mechanism that regulatory ligands, like PIP_2, might cooperate with the NTD in the regulation of SLC4 family activity.

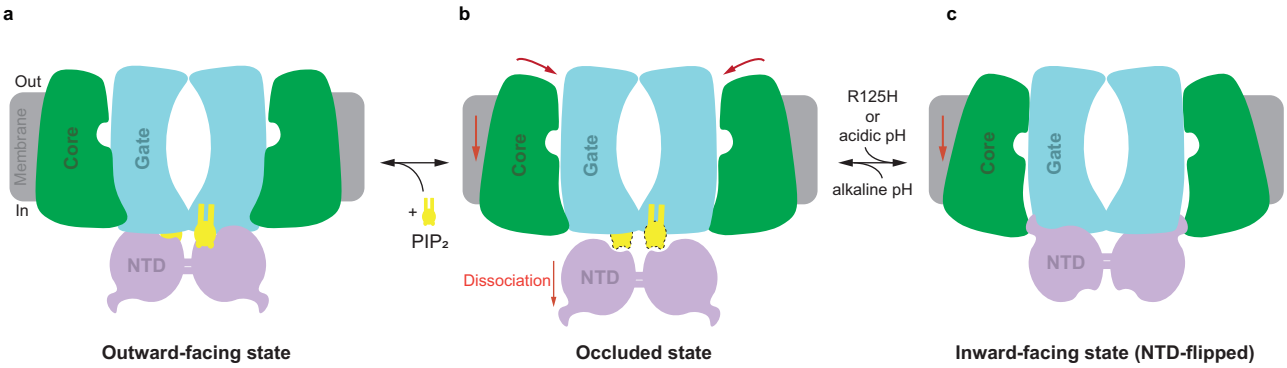

Fig. 6 | BTR1 state transition process. a BTR1 is in the outward-facing state with PIP_2 stably binding. **b** Dissociation of PIP_2 molecules from the NTDs of BTR1 after ions reach the substrate binding sites induces the rotation of the core domains, leading to the occluded state of BTR1. **c** Disruption of the interaction between PIP_2 and BTR1 due to acidic pathological condition or pathogenic mutation in the L site, triggers the flip of the NTD and the conformational change into the inward-facing state.

In summary, we present the cryo-EM structures of full-length BTR1 in the outward-facing state in complex with PIP_2 and in the inward-facing state under pathological conditions. These structures shed light on the structural basis of how BTR1 implement its transport activities. Our experimental results also provide important insights into understanding how PIP_2 participate in the conformational transition, pH sensing and functional regulation of BTR1.

Methods

Cell culture

HEK293F cells (Thermo Fisher Scientific) were cultured in suspension in Freestyle 293 medium (Gibco) supplemented with 1% fetal bovine serum (FBS) at 37 °C with 6% CO_2 and 70% humidity.

Constructs

Full-length *SLC4A11* gene (UniProtKB accession: Q8NBS3) was amplified from human HEK293 cDNA and then cloned into PCGFP-BacMam (PBM) plasmid (kindly provided by Eric Gouaux lab[24]) using EcoR1 and Xho1 restriction sites. A series of point mutations were carried out with the PBM-*SLC4A11* plasmid by the KOD-PLUS-neo enzyme (TOYOBO). To measure the plasma membrane expression of BTR1 and its mutants, we inserted a HA-tag (YPYDVPDYA) into the PBM-*SLC4A11* plasmid between aa 544 and aa 545, which is located at a flexible loop in the extracellular region of the transporter.

Expression and purification

BTR1 wild-type and R125H mutant proteins were overexpressed in HEK293F cells using the Bac-to-Bac baculovirus expression system (Invitrogen, USA). The PBM plasmids were transformed into DH10B cells to produce bacmid and then SF9 insect cells were used to mediate the package and amplification of Baculovirus. Subsequently, a 1:10 ratio of baculovirus against 293F cells was used to infect HEK293F cells and the cells were incubated at 37 °C in suspension supplemented with 1% (v/v) FBS and 5% CO_2 in a shaking incubator. Twelve hours later, 10 mM sodium butyrate was added to the culture. The cells were incubated for further 48 h before harvesting.

The HEK293F cells expressing BTR1 proteins (wild-type or R125H) were collected by centrifugation at 4000 g for 10 min and resuspended with 1 × TBS buffer (140 mM NaCl, 3 mM KCl and 30 mM Tris-HCl, pH 7.4). The resuspended cells were ultrasonically extracted after the addition of 10 mM PMSF and then centrifuged at 8000 g for 20 min to remove the cell nuclei and organelles. The supernatant was removed and centrifuged at 100,000 g for 1 h to collect the cell membrane. The precipitate was solubilized with dissolving buffer (150 mM NaCl, 20 mM Tris-HCl pH 7.4, 1% (w/v) n-dodecyl β-D-maltoside (DDM, Anatrace), and 0.2% (w/v) cholesteryl hemisuccinate (CHS, Anatrace)), and was then stirred at 100 g at 4 °C for 1 h. The mix was centrifugated at 100,000 g for 30 min and then the supernatant was collected and mixed slowly with Ni-NTA beads. Non-specifically bound protein was washed using 10 columns of purification buffer (150 mM NaCl, 20 mM HEPES, pH 7.4 or pH 5.5, and 0.01% (w/v) glyco-diosgenin (GDN, Anatrace)) in addition with 20 mM or 40 mM imidazole. The target protein was eluted using 2 columns of purification buffer in addition to 250 mM imidazole. GFP and His-tag of the eluted protein were removed by incubating with TEV protease at 4 °C overnight, and then concentrated and further purified by gel filtration (Superose 6 Increase 10/300 GL, GE Healthcare, USA). Peak fractions were collected and concentrated to nearly 10 mg/mL for cyro-EM sample preparation.

Cryo-EM sample preparation and data acquisition

The concentrated protein samples were loaded onto glow-discharged quantifoil R 1.2/1.3 200 Holey Carbon films Au 200 mesh grids and blotted with filter paper for 3 s under 100% humidity at 4 °C before being plunged into liquid ethane with a FEI Vitrobot Mark IV. A 300 kV Titan Krios electron microscopy with a Gatan K2 Summit direct electron detection camera was used for data collection. A calibrated magnification of 165kx with a pixel size of 0.821 Å was used for acquisition of movies. 8 e/pixel/s dose rate and total dose of 52.2 e/Å^2 was used. Each 4.4 s movie was dose-fractioned into 40 frames. For each protein condition, >2000 micrographs were collected for structural analysis.

Image processing

We used the cryoSPARC software for structural analysis[48]. The original movies were aligned and motion corrected with Patch motion correction step. The averaged micrographs were generated by 2× binning. The corrected micrographs were carried out with Patch CTF estimation for CTF measuring and further image selection. Bad images with inappropriate power spectra and ice thickness were deleted within the Manually Curate Exposures step. Protein particles were initially picked using Blob picker with a proper box size and then extracted from micrographs. The extracted particles were then subjected to 2D classification to generate 100 2D classes. Nearly 10–20 good 2D classes were selected to generate several initial models using the Ab-initio reconstruction step. The best initial model was used to create templates and the templates of different angles were further used for template picking. After a second round of particle extraction, 2D classification and 2D class selection, a new initial model was generated for further 3D reconstruction and refinement. Non-uniform refinement was performed to enhance the resolution. Ultimately, local refinement was carried out to optimize the 3D map to the highest resolution. We

used the 0.143 Å criterion of 'gold-standard' Fourier shell correlations (FSCs) to estimate the overall resolution within cryoSPARC. Local-resolution estimation of reconstructed maps were also determined within cryoSPARC[48].

Model building and refinement

We used alphafold[49] to build the initial models of the NTD and TMD of BTR1 and merged them in Coot[50]. The two BTR1 domains of BTR1 are similar to those of other SLC4 family members, especially TMD, as the substrate binding site is in nearly the same position. The N-terminal 1–103 residues, the flexible regions between the NTD and the TMD (reside 308 to reside 335) and the C-terminal 888–891 residues could not be built due to their flexibility. PIP_2 was built with TMD based on the density of map. We used the real-space refinement mode of phenix[51] to further refine the model.

The inward-facing state of BTR1 was built as described above. Because of insufficient density, some residues are still missing. In view of the rotation of NTD in this state, we used a different initial model. PIP_2 was not built because the density disappeared in these two models, but the rest of the steps are the same as above.

Assessment of membrane protein expression

To assess the membrane expression of the constructs encoding BTR1 and its mutants, we inserted a HA-tag (YPYDVPDYA) into the PBM-*SLC4A11* wild-type and mutant plasmids between aa 544 and aa 545, which is located on a flexible extracellular loop of the transporter. Wild-type *SLC4A11* and its mutants were transfected into HEK293F cells with polyethylenimine (PEI) (Polysciences) at a cell density of 1.5×10^6/ml. Cells were harvested 36 h after transfection. Approximately 2×10^6/ml of each cell type were collected by centrifugation at 1000 g for 1 min and washed with PBS buffer twice. Cells were then incubated with 50 µl PBS with 1% FBS (PAN Biotech) and 0.1 µl PE anti-HA.11 Epitope Tag Flow Cytometry Antibody (BioLegend) at 37 °C for 30 min. Cells were washed twice in PBS and resuspended in 500 ul PBS, and then transferred into 5 ml polystyrene round-bottom tubes for flow cytometry analysis. FITC and PE channel were detected sequentially, representing the target protein total expression (GFP) and membrane expression (PE-conjugated anti-HA), respectively. The ratio of cell numbers and fluorescence intensity of the two signals were calculated within FlowJo v10.6.2.

Electrophysiology

BTR1 constructs were transfected into FreeStyle 293 F cells using PEI at a cell density of 1×10^6 cells/ml. Cells were cultured in FreeStyle 293 Expression Medium with 1% FBS (PAN Biotech) for 24–36 h before making recordings. Currents were recorded using whole-cell mode at −55 mV or recorded at a holding potential of −55 mV and a series of 400-ms voltage pulses with 15-mV increments (−100–+50 mV) through an Axon-patch 200B amplifier (Axon Instruments, USA). Patch electrodes were pulled by a horizontal micro-electrode puller (P-1000, Sutter Instrument Co, USA) to a tip resistance of 1.0–3.0 MΩ. Pipette solution [containing (mM): 135 cesium gluconate (CsOH mixed with gluconic acid), 1 $CaCl_2$, 10 tetraethylammonium chloride (TEA-Cl), 10 EGTA, and 10 HEPES (pH 7.4, CsOH)] and bath solution [containing (mM): 140 TMACl, (or 135 TMACl and 5 NH_4Cl) 1.5 $CaCl_2$, 10 CsCl, and 10 HEPES (pH 7.4, or 6.5, 8.0, HCl)] were used for recording steady-state currents and measuring the activating effect of NH_3. Pipette solution pH was changed to 7.0 when measuring H+ currents at different pHi. Signals were acquired at 5 kHz and low-pass filtered at 300 Hz. Data were further analyzed with pclampfit 10.0 software.

Computational modeling

To gain deeper insights into the binding mechanism of PIP_2 to SLC4A11, we conducted in silico calculations. The configurations of PIP_2 were optimized at B3LYP/6−31 G* level using Gaussian 09 package. The starting configurations of the SLC4A11 and PIP_2 system for molecular dynamics (MD) simulation were attained from the cryo-EM structures. The complex was embedded in a POPC bilayer (190 and 174 POPC molecules in the upper and lower leaflet, respectively) to generate a suitable membrane system with 15 Å layers of water on both sides of the membrane and 150 mM NaCl using CHARMM-GUI[52].

MD simulation on SLC4A11/PIP_2 complex was performed with AMBER20[53] using AMBER ff99SB-ILDN, Lipid14 force field and Generalized Amber Force Field (GAFF). The topological parameters of PIP_2 were generated using RESP charge fitting in Antechamber. The particle mesh Ewald (PME) algorithm[36] was employed to compute long-range electrostatic energies, and van der Waals and Coulomb interactions were truncated at 10 Å. All hydrogen-related covalent bonds were constrained using the SHAKE algorithm.

The system firstly underwent minimization of side chains of the protein and PIP_2, respectively. 2500 steps of steepest-descent and 2500 steps of conjugate-gradient minimization then followed to remove unfavorable contacts. The system was gradually heated from 0 K to 298 K and then equilibrated for 500 ps at 1 atm in an isochoric/isothermal (NPT) ensemble with periodic boundary conditions. Temperature and pressure controls were achieved by Nosé-Hoover thermostat[54] and Berendsen barostat[55] with a frequency of 2.0 ps, respectively. Finally, the equilibrated systems were subjected to 1 µs-long production. All MD simulation processes were independently performed three times.

Calculation of binding free energies

The Molecular Mechanics Generalized Born Surface Area (MM/GBSA) approach[36] has been successfully applied to predict the binding free energy (ΔG_{bind}) in various protein-ligand complexes. Here, 1000 snapshots were extracted from the last 50 ns MD trajectory. The detailed calculations can be expressed as follows:

$$\triangle G_{bind} = \triangle H - T\triangle S \approx \triangle E_{gas} + \triangle G_{sol} - T\triangle S \quad (1)$$

$$\triangle E_{gas} = \triangle E_{ele} + \triangle E_{vdW} \quad (2)$$

$$\triangle G_{sol} = \triangle G_{pol} + \triangle G_{np} \quad (3)$$

Where ΔE_{gas}, ΔG_{sol} and $-T\Delta S$ represent the changes of binding energy in the gas phase, solvation and the conformational entropy upon binding, respectively. ΔE_{gas} includes ΔE_{ele} (electrostatic) + ΔE_{vdW} (van der Waals) potential. ΔG_{sol} contains contributions of polar (ΔG_{pol}) and nonpolar (ΔG_{np}) terms. Given that the binding conformational entropy (ΔS) is computationally expensive and of limited accuracy, we assumed that ΔG_{bind} is approximately equal to the sum of ΔE_{gas} and ΔG_{sol}.

Reporting summary

Further information on research design is available in the Nature Portfolio Reporting Summary linked to this article.

Data availability

The data that support this study are available from the corresponding authors upon request. The cryo-EM maps have been deposited in the Electron Microscopy Data Bank (EMDB) under accession codes EMD-32942 ($BTR1_{OF/APO}$), EMD-32943 ($BTR1_{OF/NH3}$), EMD-32941 ($BTR1_{IF/R125H}$), and EMD-32940 ($BTR1_{IF/5.5}$). Atomic model coordinates have been deposited in the Protein Data Bank (PDB) under accession codes 7X1I ($BTR1_{OF/APO}$), 7X1J ($BTR1_{OF/NH3}$), 7X1H ($BTR1_{IF/R125H}$), and 7X1G ($BTR1_{IF/5.5}$). Source data are provided with this paper.

References

1. Thornell, I. M. & Bevensee, M. O. Regulators of Slc4 bicarbonate transporter activity. *Front. Physiol.* **6**, 166 (2015).
2. Parker, M. D., Ourmozdi, E. P. & Tanner, M. J. Human BTR1, a new bicarbonate transporter superfamily member and human AE4 from kidney. *Biochem Biophys. Res Commun.* **282**, 1103–1109 (2001).
3. Park, M., Li, Q., Shcheynikov, N., Zeng, W. & Muallem, S. NaBC1 is a ubiquitous electrogenic Na+ -coupled borate transporter essential for cellular boron homeostasis and cell growth and proliferation. *Mol. Cell* **16**, 331–341 (2004).
4. Zhang, W., Ogando, D. G., Bonanno, J. A. & Obukhov, A. G. Human SLC4A11 is a novel NH3/H+ Co-transporter. *J. Biol. Chem.* **290**, 16894–16905 (2015).
5. Kao, L. et al. SLC4A11 function: evidence for H(+)(OH(-)) and NH3-H(+) transport. *Am. J. Physiol. Cell Physiol.* **318**, C392–C405 (2020).
6. Kao, L. et al. Multifunctional ion transport properties of human SLC4A11: comparison of the SLC4A11-B and SLC4A11-C variants. *Am. J. Physiol. Cell Physiol.* **311**, C820–C830 (2016).
7. Damkier, H. H., Nielsen, S. & Praetorius, J. Molecular expression of SLC4-derived Na+-dependent anion transporters in selected human tissues. *Am. J. Physiol. Regul. Integr. Comp. Physiol.* **293**, R2136–2146, (2007).
8. Romero, M. F., Chen, A. P., Parker, M. D. & Boron, W. F. The SLC4 family of bicarbonate (HCO(3)(-)) transporters. *Mol. Asp. Med* **34**, 159–182 (2013).
9. Lopez, I. A. et al. Slc4a11 gene disruption in mice: cellular targets of sensorineuronal abnormalities. *J. Biol. Chem.* **284**, 26882–26896 (2009).
10. Aldave, A. J. *et al*. Autosomal recessive CHED associated with novel compound heterozygous mutations in SLC4A11. *Cornea* **26**, 896–900 (2007).
11. Vithana, E. N. et al. Mutations in sodium-borate cotransporter SLC4A11 cause recessive congenital hereditary endothelial dystrophy (CHED2). *Nat. Genet* **38**, 755–757 (2006).
12. Hemadevi, B. et al. Identification of mutations in the SLC4A11 gene in patients with recessive congenital hereditary endothelial dystrophy. *Arch. Ophthalmol.* **126**, 700–708 (2008).
13. Riazuddin, S. A. et al. Missense mutations in the sodium borate cotransporter SLC4A11 cause late-onset Fuchs corneal dystrophy. *Hum. Mutat.* **31**, 1261–1268 (2010).
14. Desir, J. et al. Borate transporter SLC4A11 mutations cause both Harboyan syndrome and non-syndromic corneal endothelial dystrophy. *J. Med. Genet.* **44**, 322–326 (2007).
15. Badior, K. E., Alka, K. & Casey, J. R. SLC4A11 three-dimensional homology model rationalizes corneal dystrophy-causing mutations. *Hum. Mutat.* **38**, 279–288 (2017).
16. Chiu, A. M., Mandziuk, J. J., Loganathan, S. K., Alka, K. & Casey, J. R. High throughput assay identifies glafenine as a corrector for the folding defect in corneal dystrophy-causing mutants of SLC4A11. *Invest. Ophthalmol. Vis. Sci.* **56**, 7739–7753, (2015).
17. Arakawa, T. et al. Crystal structure of the anion exchanger domain of human erythrocyte band 3. *Science* **350**, 680–684 (2015).
18. Xia, X., Liu, S. & Zhou, Z. H. Structure, dynamics and assembly of the ankyrin complex on human red blood cell membrane. *Nat. Struct. Mol. Biol.* **29**, 698–705 (2022).
19. Vallese, F. et al. Architecture of the human erythrocyte ankyrin-1 complex. *Nat. Struct. Mol. Biol.* **29**, 706–718 (2022).
20. Zhekova, H. R. et al. CryoEM structures of anion exchanger 1 capture multiple states of inward- and outward-facing conformations. *Commun. Biol.* **5**, 1372 (2022).
21. Zhang, Q. et al. The structural basis of the pH-homeostasis mediated by the Cl(-)/HCO(3)(-) exchanger, AE2. *Nat. Commun.* **14**, 1812 (2023).
22. Huynh, K. W. et al. CryoEM structure of the human SLC4A4 sodium-coupled acid-base transporter NBCe1. *Nat. Commun.* **9**, 900 (2018).
23. Wang, W. et al. Cryo-EM structure of the sodium-driven chloride/bicarbonate exchanger NDCBE. *Nat. Commun.* **12**, 5690 (2021).
24. Goehring, A. et al. Screening and large-scale expression of membrane proteins in mammalian cells for structural studies. *Nat. Protoc.* **9**, 2574–2585 (2014).
25. Yu, X. et al. Dimeric structure of the uracil:proton symporter UraA provides mechanistic insights into the SLC4/23/26 transporters. *Cell Res.* **27**, 1020–1033 (2017).
26. Smart, O. S., Goodfellow, J. M. & Wallace, B. A. The pore dimensions of gramicidin A. *Biophys. J.* **65**, 2455–2460 (1993).
27. Iqbal, A. et al. Mutational analysis in sodium-borate cotransporter SLC4A11 in consanguineous families from Punjab, Pakistan. *PLoS One* **17**, e0273685 (2022).
28. Kodaganur, S. G. et al. Mutation analysis of the SLC4A11 gene in Indian families with congenital hereditary endothelial dystrophy 2 and a review of the literature. *Mol. Vis.* **19**, 1694–1706 (2013).
29. Czech, M. P. PIP2 and PIP3: complex roles at the cell surface. *Cell* **100**, 603–606 (2000).
30. Hansen, S. B., Tao, X. & MacKinnon, R. Structural basis of PIP2 activation of the classical inward rectifier K+ channel Kir2.2. *Nature* **477**, 495–498 (2011).
31. Buchmayer, F. et al. Amphetamine actions at the serotonin transporter rely on the availability of phosphatidylinositol-4,5-bisphosphate. *P Natl Acad. Sci. USA.* **110**, 11642–11647 (2013).
32. Hamilton, P. J. et al. PIP2 regulates psychostimulant behaviors through its interaction with a membrane protein. *Nat. Chem. Biol.* **10**, 582–589 (2014).
33. Wu, J., McNicholas, C. M. & Bevensee, M. O. Phosphatidylinositol 4,5-bisphosphate (PIP2) stimulates the electrogenic Na/HCO3 cotransporter NBCe1-A expressed in xenopus oocytes. *Proc. Natl Acad. Sci. USA* **106**, 14150–14155 (2009).
34. Thornell, I. M., Wu, J. P., Liu, X. F. & Bevensee, M. O. PIP2 hydrolysis stimulates the electrogenic Na+-bicarbonate cotransporter NBCe1-B and -C variants expressed in xenopus laevis oocytes. *J. Physiol. Lond.* **590**, 5993–6011 (2012).
35. Hong, J. H. et al. Convergence of IRBIT, phosphatidylinositol (4,5) bisphosphate, and WNK/SPAK kinases in regulation of the Na +-HCO3- cotransporters family. *Proc. Natl Acad. Sci. USA.* **110**, 4105–4110 (2013).
36. Hou, T. J., Wang, J. M., Li, Y. Y. & Wang, W. Assessing the performance of the MM/PBSA and MM/GBSA Methods. 1. The accuracy of binding free energy calculations based on molecular dynamics simulations. *J. Chem. Inf. Model.* **51**, 69–82 (2011).
37. Li, S. et al. R125H, W240S, C386R, and V507I SLC4A11 mutations associated with corneal endothelial dystrophy affect the transporter function but not trafficking in PS120 cells. *Exp. Eye Res.* **180**, 86–91 (2019).
38. Myers, E. J., Marshall, A., Jennings, M. L. & Parker, M. D. Mouse Slc4a11 expressed in Xenopus oocytes is an ideally selective H+/OH- conductance pathway that is stimulated by rises in intracellular and extracellular pH. *Am. J. Physiol. Cell Physiol.* **311**, C945–C959 (2016).
39. Quade, B. N., Marshall, A. & Parker, M. D. pH dependence of the Slc4a11-mediated H(+) conductance is influenced by intracellular lysine residues and modified by disease-linked mutations. *Am. J. Physiol. Cell Physiol.* **319**, C359–C370 (2020).
40. Ficici, E., Faraldo-Gomez, J. D., Jennings, M. L. & Forrest, L. R. Asymmetry of inverted-topology repeats in the AE1 anion exchanger suggests an elevator-like mechanism. *J. Gen. Physiol.* **149**, 1149–1164 (2017).
41. Thurtle-Schmidt, B. H. & Stroud, R. M. Structure of Bor1 supports an elevator transport mechanism for SLC4 anion exchangers. *Proc. Natl Acad. Sci. USA.* **113**, 10542–10546 (2016).
42. Dong, Y. et al. Structure and mechanism of the human NHE1-CHP1 complex. *Nat. Commun.* **12**, 3474 (2021).

43. Ung, K. L. et al. Structures and mechanism of the plant PIN-FORMED auxin transporter. *Nature* **609**, 605–610 (2022).
44. Kalli, A. C. & Reithmeier, R. A. F. Interaction of the human erythrocyte band 3 anion exchanger 1 (AE1, SLC4A1) with lipids and glycophorin A: molecular organization of the wright (Wr) blood group antigen. *PLoS Comput. Biol.* **14**, e1006284 (2018).
45. Thornell, I. M., Wu, J., Liu, X. & Bevensee, M. O. PIP2 hydrolysis stimulates the electrogenic Na+-bicarbonate cotransporter NBCe1-B and -C variants expressed in xenopus laevis oocytes. *J. Physiol.* **590**, 5993–6011 (2012).
46. Ge, J. et al. Molecular mechanism of prestin electromotive signal amplification. *Cell* https://doi.org/10.1016/j.cell.2021.07.034 (2021).
47. Drew, D. & Boudker, O. Shared molecular mechanisms of membrane transporters. *Annu. Rev. Biochem* **85**, 543–572 (2016).
48. Punjani, A., Rubinstein, J. L., Fleet, D. J. & Brubaker, M. A. cryoSPARC: algorithms for rapid unsupervised cryo-EM structure determination. *Nat. Methods* **14**, 290–296 (2017).
49. Jumper, J. et al. Highly accurate protein structure prediction with alphafold. *Nature* **596**, 583–589 (2021).
50. Emsley, P. & Cowtan, K. Coot: model-building tools for molecular graphics. *Acta. Crystallogr. D. Biol. Crystallogr.* **60**, 2126–2132 (2004).
51. Afonine, P. V. et al. Real-space refinement in PHENIX for cryo-EM and crystallography. *Acta. Crystallogr. D. Struct. Biol.* **74**, 531–544 (2018).
52. Jo, S., Kim, T., Iyer, V. G. & Im, W. CHARMM-GUI: a web-based graphical user interface for CHARMM. *J. Comput. Chem.* **29**, 1859–1865 (2008).
53. Salomon-Ferrer, R., Case, D. A. & Walker, R. C. An overview of the amber biomolecular simulation package. *Wires Comput. Mol. Sci.* **3**, 198–210 (2013).
54. Hoover, W. G. Canonical dynamics—equilibrium phase-space istributions. *Phys. Rev. A* **31**, 1695–1697 (1985).
55. Berendsen, H. J. C., Postma, J. P. M., Vangunsteren, W. F., Dinola, A. & Haak, J. R. Molecular-dynamics with coupling to an external bath. *J. Chem. Phys.* **81**, 3684–3690 (1984).

Acknowledgements

Cryo-EM data collection was supported by the Electron Microscopy Laboratory and Cryo-EM Platform of Peking University with the assistance of Xuemei Li, Zhenxi Guo, Xia Pei, Bo Shao and Guopeng Wang. P.Z. received training in cryo-EM sample preparation and data collection from Dr. Y. Mao from the School of Physics, Peking University. The paper was kindly modified by Dr. Susan Cole. This study is supported by grants to Y.Y. including National Natural Science Foundation of China (grant 82030081), the National Key Research and Development Program of China (2021YFA1300601); Shenzhen High-level Hospital Construction Fund and Shenzhen Basic Research Key Project (JCYJ20220818102811024).

Author contributions

Y.Y. initiated and guided the project. Y.L. screened constructs and purified protein with assistance from P.Z., H.C., H.S., W.W., and Z.D.; P.Z. prepared cryo-EM samples and collected cryo-EM data with assistance of D.D. and Y.L.; Y.L. processed the cryo-EM data; Y.L. built and refined the atomic models with help from D.D. and L.L.; Y.L. and P.Z. performed the whole-cell electrophysiology with assistance of D.D.; P.Z. finished the assessment of protein membrane expression; P.Z. performed the data analysis and figure drawing with assistance of D.D.; H.X. and Y.C. performed the MD simulations; Y.J. supervised the experiments. The manuscript was written by P.Z., Y.L., D.D., and Y.Y.

Competing interests

The authors declare no competing interests.

Additional information

Supplementary information The online version contains supplementary material available at https://doi.org/10.1038/s41467-023-41924-0.

Correspondence and requests for materials should be addressed to Yuxin Yin.

Peer review information *Nature Communications* thanks the anonymous reviewers for their contribution to the peer review of this work. A peer review file is available.